Nonnegative magnetoresistance in hydrodynamic regime of electron fluid transport in two-dimensional materials

Yunfan Huang and Moran Wang [*]
Department of Engineering Mechanics, Tsinghua University, Beijing 100084, China

Electron transport in ultraclean two-dimensional materials has received much attention. However, the sign of the magnetoresistance effect in various electron flow regimes remains controversial. In this work, the complete electron Boltzmann transport equation is numerically solved with the discrete ordinate method in the real space to clarify the condition of the negative magnetoresistance effect under a weak magnetic field. It turns out from the numerical results that this effect occurs only within the ballistic regime under a low electric field rather than the hydrodynamic regime. It is noteworthy that the existence of momentum-conserving scattering dramatically reverses the sign of magnetoresistance in the ballistic regime. When the electric field becomes strong enough compared to the magnetic field, its effect on the deflection of the electrons is not negligible and will lead to positive magnetoresistance in the whole parameter domain. The possible influence of boundary conditions and internal electric field models on the sign of magnetoresistance is also discussed. Our work provides insight into electron fluid transport under electromagnetic fields.

I. INTRODUCTION

In classical theory, the electric resistivity of solids increases with the rise of temperature, originating from the dominated scattering between electrons and the lattice (including defects and phonons). However, recent experiments have shown that the resistance decreases in some two-dimensional impurity-free materials at low temperatures and under confinement, such as GaAs heterostructure and graphene [1–3]. This phenomenon is called the "Gurzhi minimum", which was first predicted by Gurzhi in the 1960s [4,5]. A macroscopic hydrodynamic description with a novel property called "electron viscosity" was used to evaluate the electric resistivity by analogy with classical viscous fluid mechanics and accounted for this abnormal phenomenon successfully, which suggests the emergence of the hydrodynamic regime for electron transport [6–9]. Within the mesoscopic picture, the hydrodynamic analogy requires the dominance of momentum-conserving scattering among the bulk scatterings, which indicates that the electron-electron normal scattering may play an essential role in the electron transport in these materials. Considering that the momentum-conserving scatterings will not directly contribute to the electron transport resistance, the "real resistance" is provided by diffusive scattering at the system boundary ensuring the local equilibrium, which leads to the no-slip boundary condition in the macroscopic description. The momentum-conserving scatterings give rise to the electron viscosity, which exchanges and tends to homogenize the momentum between contiguous electron fluid elements from the macroscopic point of view. Massive studies have been implemented on this viscous electron transport, and impres-

sive experimental evidence has arisen in succession in recent years benefiting from the improvement of experimental techniques. The research interests have been extended to negative nonlocal resistance [10–15], enhanced electron conduction [2,16–18], microscale electron turbulence [19,20], hydrodynamic magnetoresistance [21–45], electron flow field visualization [15,46–52], and significant analogy in electron flow with classical fluid mechanics such as the Bernoulli effect [53], boundary layer [54], and nonlinear density waves [55].

Electron hydrodynamics focuses on the evolution of several conservative macroscopic quantities in the electron transport (such as the momentum within the hydrodynamic regime), ignores the redundant high-order microscopic information, and describes the property of the electronic system with several transport coefficients, especially the viscosity and thermal conductivity. While the controlling equation in viscous fluid mechanics is named the "Navier-Stokes equation", we will call the macroscopic hydrodynamic equation for electron the "electron Navier-Stokes equation" (eNSE). Though sharing the same notion of "hydrodynamics", electron transport has many distinct properties from the classical fluid, such as its quantum wave nature dependent on the material's concrete property, the spin/charge-induced effect resulting in the response to the external electromagnetic field, and the existence of momentum-relaxing bulk scattering leading to the bulk resistivity. Besides the "classical giant magnetoresistivity" as a spin effect, experiments have shown the giant negative magnetoresistance of the two-dimensional electron gas in nonmagnetic materials [22,24,25,36,56], and similar phenomena are found in other particle systems such as electron-hole fluid [37,38,40,57,58], which indicates a much simpler and more efficient way to regulate the electric resistance. Based on macroscopic eNSE without surplus parameters, the main result in GaAs heterostructure narrow channel is later

---
[*]Corresponding author: mrwang@tsinghua.edu.cn

successfully reproduced, which is considered as new evidence of viscous electron transport [26,28].

Numerous theoretical and numerical studies have tried to show that the negative magnetoresistance originates from the electron viscosity and marks the existence of the hydrodynamic regime of the electron transport. However, whether the negative magnetoresistance always comes from the hydrodynamic effect of electron fluid transport remains an open problem. First, the previous work mostly focused on the linear response of the electron transport to the external electric field, based on the Stokes-like eNSE [11,12,15,28,59–61]. It should be noticed that the commonly used macroscopic equations lack the consideration of the nonlinear effect of the external electric field on the electric current, which may strongly influence the sign of the magnetoresistance according to the mesoscopic analysis, as shown in Sec. V B. As well, these equations are usually obtained through phenomenological deduction or upscaling from the mesoscopic equations without a rigid evaluation of their applicability. Second, it is deduced from the study on the magnetoresistance effect based on the macroscopic eNSE that the sign of magnetoresistance dramatically reverses when the normal current flow at boundary becomes nonzero [43,62]. These studies indicate the importance of the assumed certain boundary condition and elicit another shortfall of the hydrodynamic description that it cannot reflect the mesoscopic mechanisms and detailed information, which may lead to totally different results as above.

Compared to the macroscopic eNSE, the electron Boltzmann transport equation (eBTE) presents more mesoscopic statistical details. An impressive study by Molenkamp *et al.* developed a landmark theoretical formulation based on the Boltzmann approach, and the calculation is quantitatively in agreement with their experiment within the hydrodynamic regime of electron transport in GaAs heterostructure [1]. However, the complexity of the eBTE makes the theoretical calculation rather difficult, and the solution can be obtained only under considerable simplifications in this way. For example, in previous theoretical studies, the displaced eBTE is often utilized for analysis, which focuses on the evolution of the nonequilibrium part of the distribution function, i.e., the original distribution function subtracted by the local Fermi-Dirac equilibrium distribution. In particular, in many treatments of displaced eBTE, the electric field in the angular derivative term is usually omitted for it adds complexity for the theoretical calculation and is often much smaller than the magnetic field, i.e., $E \ll v_F B$ with v_F the Fermi velocity of the material, which limits these studies within the cases of linear response of the electric current to the external electric field [12,42,63–66]. Moreover, even if the simplified linearized displaced eBTE is used, it is preferred to evaluate the qualitative pattern under assumptions on the range of determinant parameters such as the dimensionless magnetic field $\tilde{B} \ll 1$ or $\tilde{B} \gg 1$, which leaves the intermediate regime in the parameter domain a kind of "virgin land" [63]. In addition, it is quite intractable for the theoretical method to deal with electron transport when it comes to complex geometry and nontrivial materials.

The present work studies the sign of magnetoresistance of electron transport in different regimes based on the dis-

crete ordinate method (DOM), which numerically solves the eBTE in the real space. The essential mesoscopic details are fully considered in our approach with a short revisit of the eNSE, and the advantage of the upwind scheme for the evolution equation is taken to extend the parameter range when solving the stationary eBTE. The remainder of this paper is organized as follows. In Sec. II the system setup and the two-dimensional electron Boltzmann formulation are given. In Sec. III we present the numerical algorithm, followed by the verification benchmark in Sec. IV. Section V gives the results of the magnetoresistance phase diagram and representative magnetoresistance curves and discusses the nonlinear effect of the external electric field on the electric current. Details of the construction of the DOM algorithm and the derivation of the macroscopic eNSE solution are given in Appendixes A and B, respectively.

II. BOLTZMANN FORMULATION

A. Two-dimensional electron Boltzmann equation

Under the quasiclassical approximation, the nonequilibrium transport of electrons is described by the following mesoscopic original eBTE:

$$\frac{\partial f}{\partial t} + \boldsymbol{v} \cdot \frac{\partial f}{\partial \boldsymbol{r}} + \frac{\boldsymbol{F}}{\hbar} \cdot \frac{\partial f}{\partial \boldsymbol{k}} = C(f), \tag{1}$$

where $f(\boldsymbol{r}, \boldsymbol{k})$ is the average occupation number; $\boldsymbol{v} = \nabla_{\boldsymbol{k}} \varepsilon_{\boldsymbol{k}} / \hbar$ the group velocity of the Bloch electron; $\boldsymbol{F} = (-e)(\boldsymbol{E} + \boldsymbol{v} \times \boldsymbol{B})$ the total force applying to a single electron with charge $-e$, including the external electromagnetic field and the electrostatic force between the electrons; and $C(f)$ the scattering term, whose explicit form will be presented in Sec. II B. In this work, we focus only on the two-dimensional materials whose energy dispersion is approximate of the parabolic form, i.e., $\varepsilon_{\boldsymbol{k}} = E_{\text{bottom}} + \hbar^2 \boldsymbol{k}^2 / (2m^*)$, which results in $\hbar \boldsymbol{k} = m^* \boldsymbol{v}$. Here E_{bottom} is the energy level at the bottom of the conductive band, and m^* is the effective mass of the band electron.

The nonequilibrium distribution function is first written in two parts, $f(\boldsymbol{r}, \boldsymbol{k}) = f^{\text{eq}}(\boldsymbol{r}, \varepsilon_{\boldsymbol{k}}) - (\partial f^{\text{eq}} / \partial \varepsilon) \chi(\boldsymbol{r}, \boldsymbol{k})$, in which $f^{\text{eq}} \equiv f^{\text{eq}}_{\varepsilon_{\boldsymbol{k}}}(\boldsymbol{r}) = 1/(\exp\{\beta[\varepsilon_{\boldsymbol{k}} - \mu(\boldsymbol{r})]\} + 1)$ is the local equilibrium distribution of electron in the Fermi-Dirac form with $\beta = 1/k_B T(\boldsymbol{r})$, and χ is the approximate energy displacement of the distribution function. Substituting the above decomposition into Eq. (1), we obtain the displaced eBTE,

$$\frac{\partial \chi}{\partial t} + \boldsymbol{v} \cdot \frac{\partial \chi}{\partial \boldsymbol{r}} + \frac{\boldsymbol{F}}{\hbar} \cdot \frac{\partial \chi}{\partial \boldsymbol{k}} + S_{\mathcal{E},T} + S_{\varepsilon} = C_{\delta}(\chi), \tag{2}$$

where $C_{\delta}(\chi)$ is the scattering term whose explicit form will also be provided in Sec. II B; the source terms $S_{\mathcal{E},T}$ for the macroscopic nonequilibrium potential gradient and S_{ε} for the high-order effect of energy displacement are defined by

$$S_{\mathcal{E},T} = \left\{ [(-e)\boldsymbol{E} - \nabla_{\boldsymbol{r}}\mu] - \frac{\varepsilon_k - \mu}{T} \nabla_{\boldsymbol{r}} T \right\} \cdot \boldsymbol{v},$$

$$S_{\varepsilon} = (-e)\boldsymbol{E} \cdot \boldsymbol{v} \left(-\beta\chi \tanh \frac{\beta(\varepsilon_k - \mu)}{2} \right). \tag{3}$$

Since the electrostatic force is considered to be greater than the pressure from the concentration gradient and the temperature effect in this work, the chemical potential and

temperature gradient terms in $S_{\mathcal{E},T}$ and the high-order effect S_ε are neglected. Thus, Eq. (2) can be simplified as follows:

$$\frac{\partial \chi}{\partial t} + v_{\rm F} \boldsymbol{e}_\rho \cdot \frac{\partial \chi}{\partial \boldsymbol{r}} + \frac{\boldsymbol{F} \cdot \boldsymbol{e}_\varphi}{m^* v_{\rm F}} \frac{\partial \chi}{\partial \varphi} + e v_{\rm F} \boldsymbol{E} \cdot \boldsymbol{e}_\rho = C_\delta(\chi), \quad (4)$$

where $\boldsymbol{e}_\rho = (\cos\varphi, \sin\varphi)$, $\boldsymbol{e}_\varphi = (-\sin\varphi, \cos\varphi)$. It is seen from Eq. (4) that the electric field serves as the external source term which drives the other terms on the l.h.s. to drift in the phase space, while the scattering term on the r.h.s. tends to make local equilibrium. The original form Eq. (1) and the displaced form Eq. (4) of the Boltzmann equation lay the foundation of the following sections.

B. Bulk scattering model and the boundary condition

In order to make a complete Boltzmann equation problem, the bulk scattering term and the boundary condition will be discussed in this section, which respectively correspond to the electron's bulk and boundary scattering.

When dealing with the bulk scattering in the electron hydrodynamics problem, it is essential whether the certain scattering conserves the total momentum of electrons. The scattering events can be divided into two types: the momentum-conserving scattering and the momentum-relaxing ones. The former refers to electron-electron normal scattering, while the latter include electron-impurity scattering, electron-phonon scattering, and Umklapp electron-electron scattering. By analogy with Steinberg's momentum-conserving single-relaxation-time approximation model for electron transport [67] and Callaway-BGK's double-relaxation-time approximation model for phonon hydrodynamics [68–71], here we present the double-relaxation-time model for electron hydrodynamics,

$$C(f) = C_{\rm MR}(f) + C_{\rm MC}(f)$$
$$\equiv -\frac{f - f^{\rm eq}_{\varepsilon_k}(\boldsymbol{r})}{\tau_{\rm MR}} - \frac{f - f^{\rm eq}_{\varepsilon_k - \hbar\boldsymbol{k}\cdot\boldsymbol{u}}(\boldsymbol{r})}{\tau_{\rm MC}}, \quad (5)$$

in which the first r.h.s. term corresponds to the momentum-relaxing scattering that conserves the local number density, while the second r.h.s. term corresponds to the momentum-conserving scattering that conserves both the local number density and the local momentum; $\boldsymbol{u}$ is the macroscopic local drift velocity of the electron fluid element; and $\tau_{\rm MR(MC)}$ is the relaxation time of momentum-relaxing (momentum-conserving) scattering. With the definition of χ, we obtain the displaced form of the scattering term in Eq. (4) from Eq. (5),

$$C_\delta(\chi) = C_{\delta,{\rm MR}}(\chi) + C_{\delta,{\rm MC}}(\chi)$$
$$\equiv -\frac{\chi - P_0[\chi]}{\tau_{\rm MR}} - \frac{\chi - P_{0,\pm 1}[\chi]}{\tau_{\rm MC}}, \quad (6)$$

where $P_{0,\pm 1}[\chi] = P_0[\chi] + P_1[\chi]\cos\varphi + P_{-1}[\chi]\sin\varphi$ and $P_i[\chi]$ $(i = 0, \pm 1)$ are the projectors that project the displaced distribution function $\chi(\boldsymbol{r}, \varphi)$ onto the bases $\{1, \cos\varphi, \sin\varphi\}$ respectively [see Eq. (7)].

$$P_0[\chi] = \int_0^{2\pi} \frac{d\varphi}{2\pi} \chi,$$

$$P_1[\chi] = \int_0^{2\pi} \frac{d\varphi}{\pi} \chi \cos\varphi, \quad P_{-1}[\chi] = \int_0^{2\pi} \frac{d\varphi}{\pi} \chi \sin\varphi. \quad (7)$$

The boundary scattering is modeled by two components, i.e., specular scattering and diffusive scattering. The specular scattering coefficient $p_{\rm s}$ is defined as the ratio of the electrons that experience the specular scattering to all the incident electrons onto the boundary. In Fuchs model $p_{\rm s}$ is constant, while in the Fuchs-Soffer model $p_{\rm s}(\varphi_{\rm i}) = \exp[-(\alpha_{\rm bd}\sin\varphi_{\rm i})^2]$, where $p_{\rm s}$ is dependent on the incident angle between the incident direction and the boundary and $\alpha_{\rm bd}$ is the parameter derived from the microscopic model [72,73]. The generalized boundary scattering model is written as follows:

$$\chi(\boldsymbol{r}_0, \theta) = \int_0^\pi d\theta' r(\theta, \theta') \chi(\boldsymbol{r}_0, \theta'), \theta' \in (-\pi, 0), \quad (8)$$

where $\boldsymbol{r}_0$ is the boundary point, and $r(\theta, \theta')$ is called "the scattering kernel", which represents the probability of the electrons incoming from $\theta' \in (0, \pi)$ and reflecting along $\theta \in (-\pi, 0)$. In this work, the angle is the direction angle in the local right-handed boundary coordinate system $(\boldsymbol{e}_{\rm t}, \boldsymbol{e}_{\rm n})$, which is defined by the tangential direction $\boldsymbol{e}_{\rm t}$ and outer normal direction $\boldsymbol{e}_{\rm n}$. Now the scattering kernel of Fuchs and Fuchs-Soffer boundary model can be written in the following compact form:

$$r_{\rm F(-S)} = p_{\rm s}(\theta')\delta(\theta + \theta') + \frac{1 - p_{\rm s}(\theta')}{\pi}. \quad (9)$$

Note that the boundary condition with scattering kernel above conserves the particle number at the boundary, i.e., the number of incident electrons equals the outcoming ones, which can be expressed as $\int_\pi^{-\pi} r(\theta, \theta') d\theta = 1$.

III. DISCRETE ORDINATE METHOD

Many numerical methods have been developed to obtain the quantitative results of eBTE efficiently, including the method of characteristics, finite volume method, DOM in wave vector space, lattice Boltzmann method, and test particle method [19,21,31,33,74–85]. These methods could be divided into two categories: discrete approach and direct simulation. The former ones discretize and solve the eBTE in different ways, while the latter track and simulate the motions of electrons directly, which makes the eBTE solved but is more time-consuming. Since we focus only on the steady electron flow in the two-dimensional straight channel with infinite length and streamwise translational symmetry, a rather simple discrete method is established to numerically solve the eBTE, i.e., DOM in the real space, by analogy with the DOM to solve phonon Boltzmann transport equation [86,87]. Note that it is pretty similar to deal with the transient electron flow in the finite-length straight channel, which will not be covered in this work.

As shown in Fig. 1, we focus on the two-dimensional electronic system with the current flows along the x-axis, a width W in the transverse direction, and an approximate infinite length, where the length of the system in the direction x is much larger than W. With the reference quantities including the absolute value of single-electron charge e, the Fermi energy $E_{\rm F}$, the Fermi velocity $v_{\rm F}$, the channel width W, and other derived quantities $B_0 = E_{\rm F}/(e v_{\rm F} W)$ and $E_0 = E_{\rm F}/(e v_{\rm F})$, the displaced eBTE (4) with double-relaxation-time approximation (6) is nondimensionalized. For the sake of convenience,
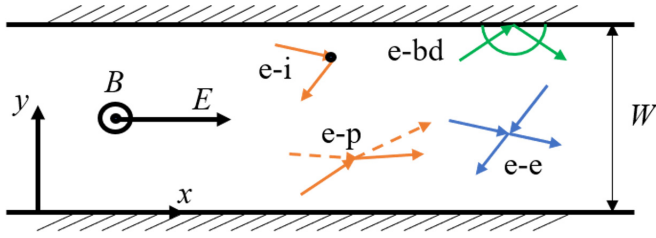
FIG. 1. System configuration.

the original notations are retained to denote the respective dimensionless quantities. With the condition of streamwise translational symmetry and steady flow, we obtain the dimensionless eBTE as follows:

$$\sin\varphi\frac{\partial\chi}{\partial y} + F_{\text{ext}}\frac{\partial\chi}{\partial\varphi} + \boldsymbol{E}\cdot\boldsymbol{e}_\varphi = C_\delta(\chi). \quad (10)$$

Here $F_{\text{ext}} = -(1/2)(\boldsymbol{E} + \boldsymbol{e}_\rho \times \boldsymbol{B})\cdot\boldsymbol{e}_\varphi$ and the external field is supposed to be uniform and stationary.

The uniform grid and the Gauss points are used to discrete the spatial coordinate and the angular coordinate, respectively. The derivatives are discretized by applying the upwind scheme, while the integrals are calculated using Gauss quadrature. Then the iteration scheme is derived as follows:

$$\chi^{(n+1)} = \frac{1}{1+\alpha+\beta}\left(D_\alpha^{(n)} + D_\beta^{(n)} - l_{\text{eff}}\boldsymbol{E}\cdot\boldsymbol{e}_\rho + I_{\text{scat}}^{(n)}\right), \quad (11)$$

where the subscripts "n"/"n + 1" denote the quantities before/after the iteration, $l_{\text{eff}} = (l_{\text{MR}}^{-1} + l_{\text{MC}}^{-1})^{-1}$ the effective relaxation path of electrons (which is approximately the mean-free path) with $l_{\text{MR(MC)}} = v_F\tau_{\text{MR(MC)}}$, α, β the numerical parameters, and $D_\alpha^{(n)}$, $D_\beta^{(n)}$, $I_{\text{scat}}^{(n)}$ the discrete forms of the spatial derivative term, the angular derivative term, and the scattering term, respectively. See Appendix A for the details of the definition of numerical parameters and the deduction of the iteration scheme, as well as the comparative discussion of the applied numerical method with others.

The macroscopic quantities with dimensions are calculated from the following expressions:

$$n_\delta(\boldsymbol{r}, t) = \int (f - f^{\text{cq}})\frac{2\,d^2\boldsymbol{k}}{(2\pi)^2} = DP_0[\chi],$$

$$\boldsymbol{j}(\boldsymbol{r}, t) = \int (-e)\boldsymbol{v}(f - f^{\text{eq}})\frac{2\,d^2\boldsymbol{k}}{(2\pi)^2}$$

$$= (-e)\frac{Dv_F}{2}(P_1[\chi], P_{-1}[\chi])^T,$$

$$\boldsymbol{u}(\boldsymbol{r}, t) = \frac{\boldsymbol{j}(\boldsymbol{r}, t)}{(-e)n(\boldsymbol{r}, t)} \simeq v_F\frac{(P_1[\chi/E_F], P_{-1}[\chi/E_F])^T}{2}. \quad (12)$$

Here $n \simeq DE_F$ is the surface density of electron number and $D = m^*/(\pi\hbar^2)$ is the density of electron states. Notice that the electrostatic field $\boldsymbol{E}$ in the iteration equation is the superposition of the external electric field and the "internal" self-consistent electric field under Hartree-Fock approximation, obtained from the Poisson equation $\nabla \cdot \boldsymbol{E} = (-e)n_\delta/\epsilon$ with ϵ the electric permittivity. The electric resistance along the flow direction, i.e., the x-axis, is calculated by $R \equiv R_{xx} = \rho_{xx}l_x/W = (E_xl_x)/(j_xW)$, in which j_x and $l_x = 1$ m is the

electric current density and prescribed length along the x-axis. Thus, the reference electric resistance is defined as

$$R_0 = \frac{\rho_{xx,0}l_x}{W} = \frac{m^*l_x}{ne^2\tau_{\text{MR}}W}. \quad (13)$$

Note that there is a distinct difference between the concept of the resistance and the resistivity that the former is a bulk concept, while the latter is for the whole system with certain geometry effects, especially boundary effects. Therefore, we will pay attention only to the electric resistance in this work.

To summarize, the DOM algorithm can be described as follows:

(1) Set the environment including material properties and characteristic length of the case and initialize the displaced distribution function $\chi(y, \varphi)$.

(2) Calculate the macroscopic quantities corresponding to the displaced distribution function $\chi^{(n)}$ using Eq. (12) and then compute the internal electric field.

(3) Utilize Eq. (11) and the respective boundary condition (8) to obtain the new displaced distribution function $\chi^{(n+1)}$.

(4) Calculate the new macroscopic quantities of the new displaced distribution function. If the difference is less than the prescribed precision, continue; otherwise, return to step 2.

(5) Calculate the macroscopic transport property using the final result of the displaced distribution function. End.

IV. BALLISTIC-DIFFUSIVE EFFECT

In the bulk materials under a small potential gradient, the macroscopic transport obeys the classical linear diffusion law such as Ohm's law $j = -\sigma\partial\phi_{\text{ele,chem}}/\partial x$ for electrochemical charge transport and Fourier's law $q = -k\partial T/\partial x$ for heat transport. One mechanism that is not included in those equations is ballistic transport, which becomes important when the sample size is smaller than the mean-free path of the particle. Also, another new type of diffusion named "the viscous diffusion" cannot be ignored when the momentum-conserving scattering rate is larger than the momentum-relaxing scattering related to the classical diffusion, which cannot be captured precisely by simply adding a viscous term into the original form of classical diffusion law as shown in this section. In essence, the ballistic-diffusive effect refers to the deviation from the prediction of the classical diffusion law when the ballistic transport and/or viscous diffusion becomes important. Under such conditions, it is required to use the mesoscopic BTE to precisely describe the above phenomena in detail. In this section, we will study the ballistic-diffusive effect numerically and verify the DOM algorithm through the comparison between the numerical DOM solution and the theoretical solution from the literature [1].

The ballistic-diffusive effect is the result of the competition of the following three mechanisms: ballistic transport, Ohmic diffusion, and viscous diffusion. When one of these effects dominates, the electron transport is said to lie in the respective regime. (1) The ballistic effect ($W \ll l_{\text{MR}}, l_{\text{MC}}$) in electron transport is analogical to the Knudsen effect in gas transport. Since the sample size is less than the mean-free path of electrons, electron-boundary scattering will dominate the transport and the electrons inside the bulk domain will experience the strong nonequilibrium and nonlocal transport.
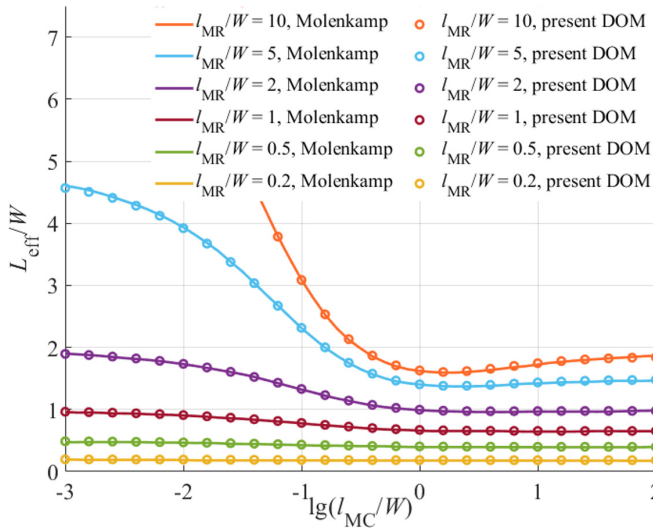
FIG. 2. Influence of momentum-relaxing scattering on the dimensionless conductivity curve ($p_s = 0$). The circles and lines are the dimensionless conductivity obtained by the numerical simulation from the present DOM algorithm and the theoretical calculation from the original literature [1], respectively. The agreement between these two series of results successfully verifies our DOM algorithm (also seen from Figs. 3 and 4). It is shown that the conductivity minimum only occurs when the momentum-relaxing scattering ($\sim l_{MR}^{-1}$) is weak enough compared to the boundary scattering rate ($\sim W^{-1}$), which indicates the mesoscopic mechanism of the Gurzhi effect as a kind of ballistic-diffusive effect.

(2) The Ohmic diffusive effect ($l_{MR} \ll W$) will lead to the Gurzhi effect at room temperatures [4]. Electron-phonon scattering dominates, and the electrons will lose energy during the transport, which is transmitted to the lattice through the scattering and eventually dissipate into the environment. This provides the classical dissipative mechanism of electric conduction in metal under room temperatures. (3) The viscous diffusive effect ($l_{MC} \ll W \ll l_{MR}$) will result in the Gurzhi effect at low temperatures [4,6]. The momentum-conserving scattering dominates the transport and conserves the total momentum of electrons, for which the electron flow behaves like classical fluids.

The case is chosen from the milestone paper by Molenkamp et al. [1]. Since the dimensionless quantities are utilized in our numerical simulation, the specific values of the material properties such as the effective mass of band electron and Fermi energy will not influence the result. In addition, considering that we concentrate only on the linear response of electron transport to the external electric field in this section, the dimensionless electric field is simply set to 10^{-6} to reduce the numerical errors. The results are shown in Figs. 2–4, with the dimensionless electric conductivity $L_{eff} = m^* v_F \sigma_{xx}/(ne^2) = m^* v_F/(ne^2 \rho_{xx})$ and electron fluid velocity $l_{eff} = u_x(mv_F/eE_x)$ defined as in [1].

Comparing the DOM numerical solutions with the theoretical solutions from literature in these figures, it is shown that our DOM algorithm passes the verification test. To emphasize the characteristics of the ballistic-diffusive effect, here we take only Fig. 4 as an example, which presents the velocity
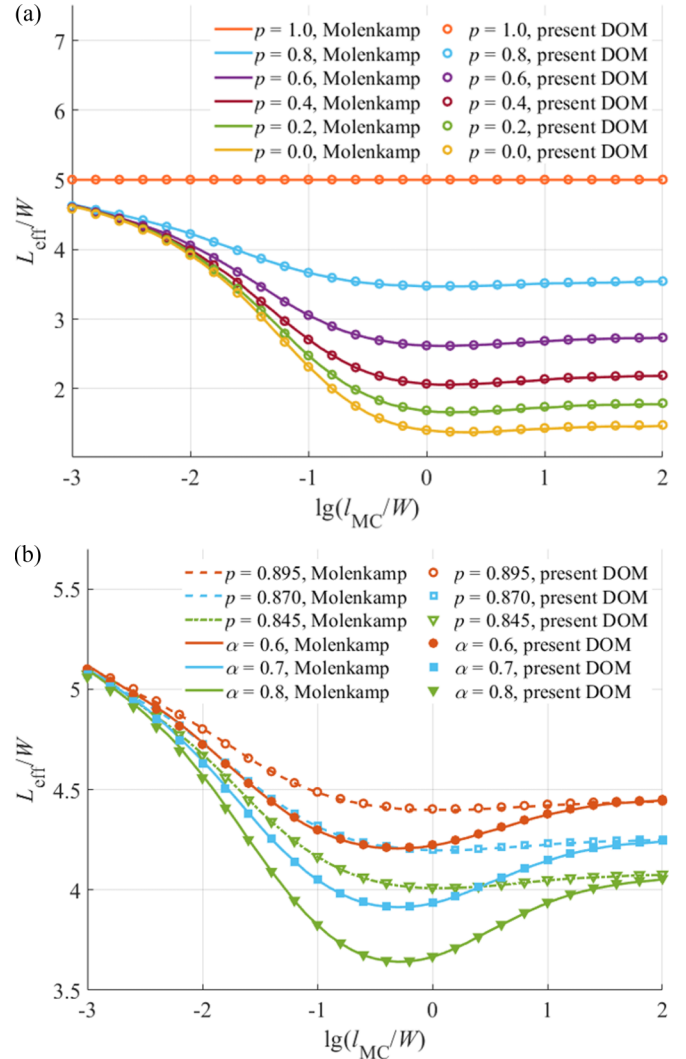

FIG. 3. Influence of the specular coefficient $p \equiv p_s$ and $\alpha \equiv \alpha_{bd}$ on the dimensionless conductivity curve under Fuchs model [$l_{MR} = 5.0W$, in (a)] and F-S model [$l_{MR} = 5.5W$, in (b)]. The comparison between the two subfigures shows that the nonuniform boundary scattering condition [$p_s(\varphi_i) = \exp[-(\alpha_{bd} \sin \varphi_i)^2]$ in (9)] acts as a necessity for the remarkable conductivity minimum, as discussed in [1].

profile in different flow regimes. As seen in the figure, in the ballistic regime ($l_{MC}/W \gg 1$), the flow is almost uniform, and there exists the velocity slip at the boundary, originating from the specular component in the electron-boundary scattering model (9). As l_{MC}/W becomes smaller, the flow profile is more and more parabolic similar to the Poiseuille flow due to the dominated momentum-conserving scattering. Electron viscosity emerges from the frequent random scatterings between the electrons. When l_{MC}/W becomes much smaller than l_{MR}/W, the flow reaches the Ohmic regime, in which the velocity inside the channel is limited by the momentum-relaxing scattering and becomes uniform. Note that the velocity nearly vanishes at the boundary due to the decreased slip length (also see Appendix B).

The comparison between the DOM results of mesoscopic eBTE and the macroscopic theoretical solution is then
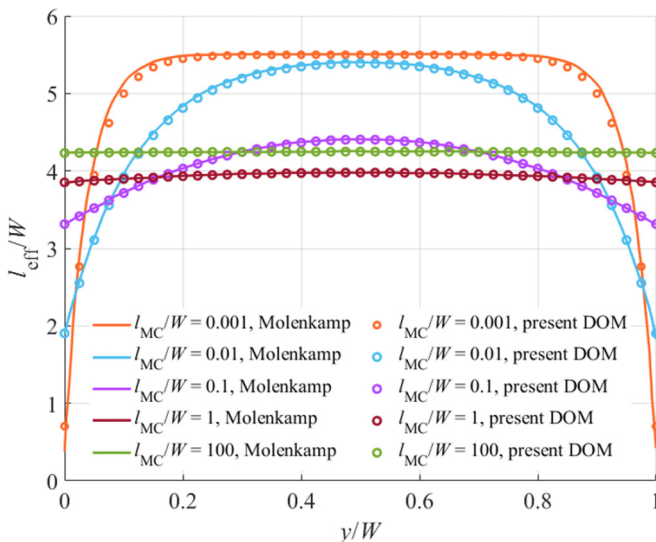
FIG. 4. Influence of momentum-conserving scattering on the dimensionless flow profile under F-S model ($l_{MR} = 5.5W$, $\alpha_{bd} = 0.7$). l_{eff}/W is the dimensionless local velocity of the electron fluid along the flow direction. In the ballistic regime where the momentum-conserving and momentum-relaxing scattering are both infrequent, the electron transport is dominated by the boundary scattering and presents the uniform flow profile. As the momentum-conserving scattering rate becomes large enough, when the momentum-relaxing scattering is not strong ($l_{MC} \ll W \ll l_{MR}$), the momentum exchange between the electrons is enhanced and nonzero viscosity emerges under the double-relaxation-time model of eBTE. As a result, the electrons act as the viscous fluid and lead to the Poiseuille-like parabolic flow profile if the sample is "impurity-free". Otherwise, the velocity inside the channel will be limited by the so-called Drude velocity induced by the strong momentum-relaxing scattering.

implemented, taking the electron two-dimensional parallel shear flow as an example. The deduction of macroscopic solutions to eNSE is given in Appendix B. The conductivity curves under different specular boundary scattering coefficients and momentum-relaxing scattering rates are shown in Figs. 5(a) and 5(b), respectively. It is indicated that when $p_s \ll 1$ and $l_{MC}/W \simeq 0.01$, the macroscopic solution matches well with the mesoscopic numerical solution. The reason for the ineffectiveness of eNSE beyond that scope (a larger p_s or a smaller sample) is that the nonequilibrium of electron transport will become stronger so that the macroscopic equation cannot describe the ballistic effect very well, with the relative errors of more than 20% compared to the DOM results [Fig. 5(b)]. Even for the cases with $p_s = 0$ and $l_{MC}/W \ll 1$, the macroscopic theoretical solution is still about 10% larger than the DOM results when $l_{MR}/W \gg 1$ [Fig. 5(a)]. This results from the approximations in the macroscopic equation, such as the ignorance of high-order Fourier coefficients in the deduction [12]. Therefore, we can obtain the adequacy of the macroscopic Eq. (A4), i.e., $p_s \ll 1$ and $Kn_{eff} \equiv l_{eff}/W \lesssim 0.01$. This also implies that eNSE is not always accurate even for the case without magnetic fields, especially when the nonequilibrium effect is strong due to the specular boundary scattering and weak momentum-relaxing scattering.
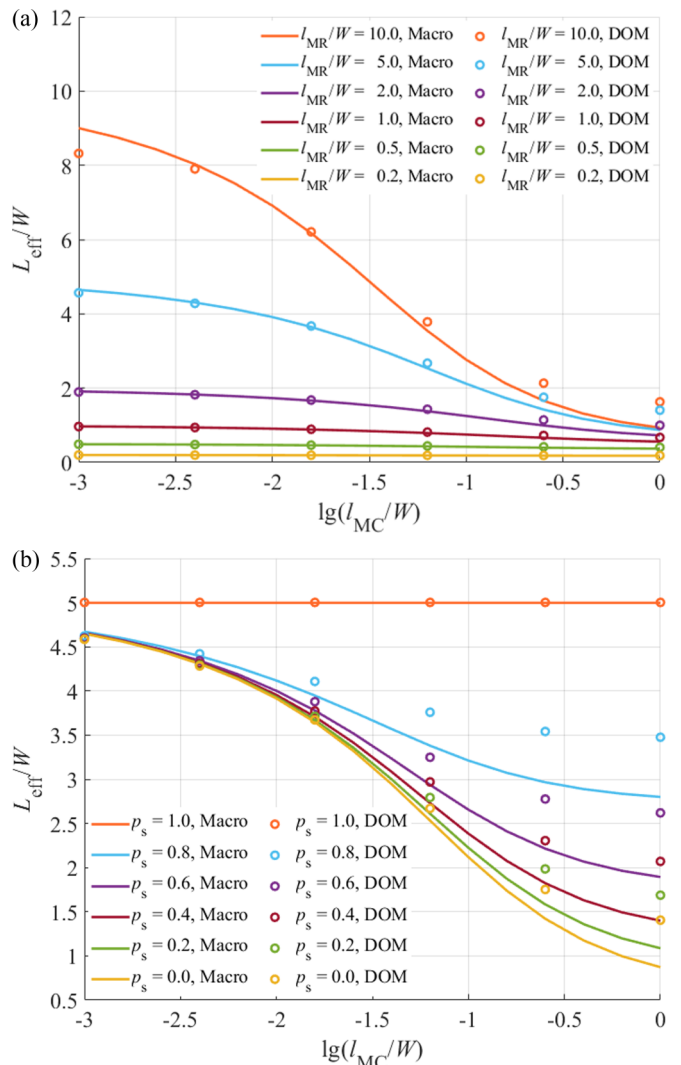

FIG. 5. Comparison between macroscopic theoretical solution (the solid lines) and mesoscopic numerical solution (the circles). Here the specular scattering coefficient p_s denotes the ratio of the electrons that experience the specular scattering to all the incident electrons onto the boundary. In particular, $p_s = 1$ corresponds to the specular reflection, while $p_s = 0$ means the uniform backscattering at the boundary. (a) $p_s = 0$; (b) $l_{MR}/W = 5$. It turns out that only when the momentum-conserving scattering rate is large and the specular boundary scattering is weak enough can the macroscopic eNSE describe the electron transport without magnetic field quite accurately.

V. MAGNETORESISTANCE EFFECT

A. Simplified case: Linearized eBTE

Now we turn to the magnetoresistance effect, i.e., the additive resistance after the magnetic field applying to the electron system under electric fields. Based on Eq. (10), the electric field in the force term F_{ext} is omitted to make comparisons with previous studies in this subsection. Under this condition, the electric current response will be linear to the external electric field, i.e., the eBTE is "linearized" and the magnetoresistance is irrelevant to the electric field itself, which has been verified by our DOM simulation. Therefore, the
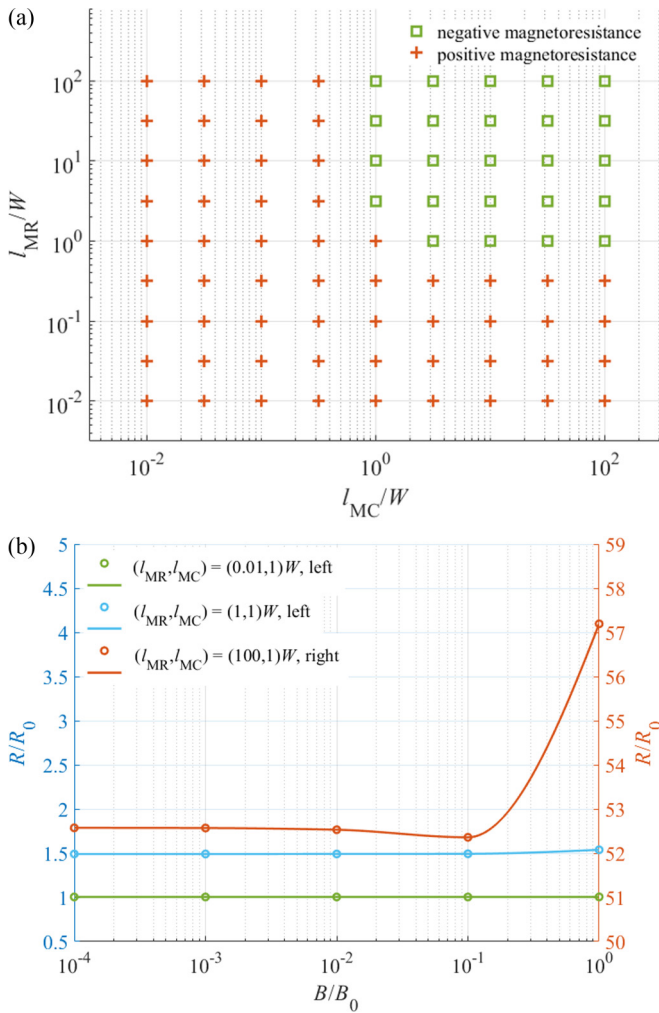
FIG. 6. Phase diagram (a) and exemplars (b) for the magnetoresistance curves under weak magnetic field, within the context of the linearized eBTE. Dots are the DOM results, while the lines are guides for the eye. It is shown from the phase diagram that the negative magnetoresistance occurs only in the ballistic regime. The typical results for $l_{MC} = W$ are shown in (b), and note that the blue curve is slightly decreasing when the dimensionless magnetic field is less than 0.1.

dimensionless electric field is set to 10^{-6} to minimize inaccuracy. The Poisson equation and Fuchs model with $p_s = 0$ are utilized to calculate the internal electric field and to maintain the particle number conservation at the boundary, respectively.

As shown in the phase diagram in Fig. 6, it is found that under a weak magnetic field, negative magnetoresistance occurs only within the ballistic regime. This is a quite surprising result, especially when compared with the previous studies on electron hydrodynamic magnetoresistance through the macroscopic hydrodynamic approach based on the eNSE [28], which demonstrates that the magnetoresistance in the hydrodynamic regime should be negative. Considering the hydrodynamic eNSE is usually obtained through phenomenological deduction with physical intuition or upscaling from the mesoscopic equations with significant simplification, its applicability has been verified with the mesoscopic eBTE in Sec. III, and it is shown the eNSE is not always accurate even

in the case without magnetic fields, which leaves an open question whether the hydrodynamic eNSE in the present form can describe the electron magnetotransport reasonably. While some mesoscopic numerical method based on the eBTE also gives the negative hydrodynamic magnetoresistance [81], the numerical algorithm has not been clarified in detail, and the ballistic results in the literature also have several discrepancies with previous studies [88].

The exemplars for $l_{MC} = W$ are shown in Fig. 6(b). It is qualitatively consistent with the theoretical evaluation in [63] within the so-called ballistic-hydrodynamic regime ($l_{MR}/W > l_{MC}/W \gg 1$) and under a relatively weak magnetic field ($\tilde{B} \ll (l_{MC}/W)^2$). From a classical microscopic view, the negative ballistic magnetoresistance is due to an increase of the mean length of the electron trajectories by which electrons move from one edge to another. One may expect that the Lorentz force will bend the particle trajectories, which enhances the electron-boundary scattering, decreases the mean-free path, and then results in a positive magnetoresistance. However, when the momentum-conserving scattering exists, part of the electrons will first collide with other electrons, which leads to a nonlocal effect and suppresses the backscattering at the boundary, as shown in [63]. Combined with the positive magnetoresistance results in the hydrodynamic regime, it is again indicated that the negative magnetoresistance under weak magnetic fields in the experiments could also be originated from the ballistic-hydrodynamic effect rather than merely the hydrodynamic transport.

The magnetoresistance curves under different regimes are further considered in detail, as shown in Fig. 7. Notice that the y-axis is the resistance along the channel, with R_0 defined in Eq. (13). Considering the resistance around zero magnetic fields, when l_{MR} is smaller than the channel width, i.e., in the Ohmic regime as shown in Fig. 7(a), it is not sensitive to l_{MC} when l_{MC} is larger than the channel width, which agrees with the property of the Ohmic flow. On the contrary, when l_{MR} is getting larger as shown in Figs. 7(b) and 7(c), the resistance behaves nonmonotonically with the increase of l_{MC}.

It is noteworthy to point out that there are several discrepancies between our results and the previous studies in the ballistic regimes. First, slightly negative magnetoresistance is found in the ballistic regime, while this value was thought to be positive under weak magnetic fields [81,89]. Since this local minimum occurs around $\tilde{B} \ll 1$, few numerical studies have focused on this parameter range, so this remains an open problem. Second, the maximum point has been believed to occur at $B/B_0 \simeq 1.1$ [81,88] or $B/B_0 \simeq 2$ [89,90], which remains controversial, while our results indicate that this value occurs at about $B/B_0 \simeq 100$ [see Fig. 7(c)]. For technical details, a random and direct simulation technique was used to make the eBTE solved in [88], which, however, brings about considerable inaccuracies for an intermediate strength magnetic field compared to our deterministic DOM simulation. Also, it is essential to keep the term $P_0[\chi]$ considering the symmetry breaking under a magnetic field as in this work, while it is omitted in the theoretical calculation of [89]. One may suggest the following conjecture on the mechanism side for the discrepancies above. As the previous paragraph shows, the existence of momentum-conserving scattering
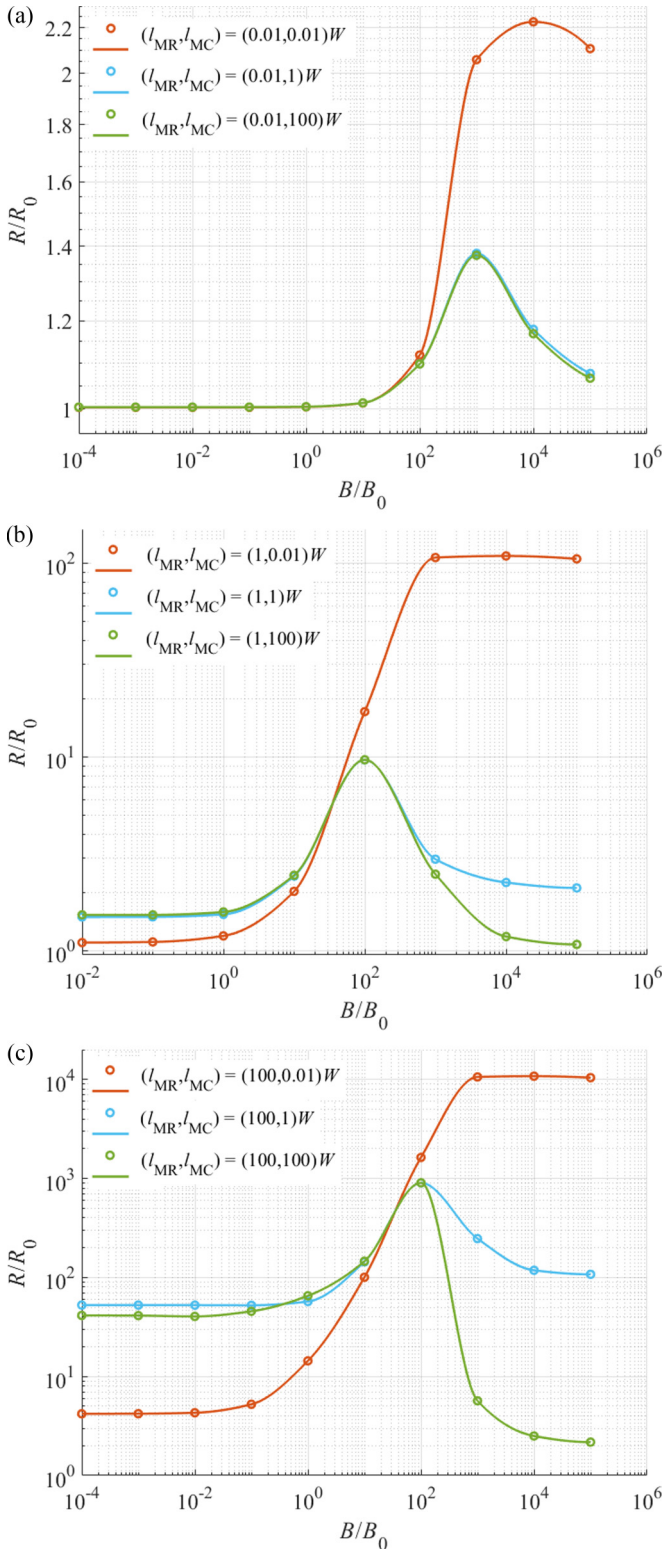
FIG. 8. Phase diagram for the magnetoresistance curves under weak magnetic field and low electric field ($E/E_0 = 10^{-6}$), within the context of complete eBTE. It is shown from the phase diagram that the negative magnetoresistance occurs only in the ballistic regime with a low electric field. When the electric field becomes larger, the whole parameter domain of ($l_{\mathrm{MR}}, l_{\mathrm{MC}}$) shows positive magnetoresistance.

B. Full formulation: Complete eBTE

As elaborated in the introduction part, the electric field in F_{ext} is usually ignored to simplify the calculation [see Eq. (10)], which, of course, has already been able to cover many of the present experiment setups. However, when the electric field is compared to the magnetic field, especially for the cases when the magnetic field is weak enough, it is not reasonable to ignore its effect on magnetoresistance, and this nonlinear effect has not been discussed by previous studies to our best knowledge. In this subsection, we will retain the electric field in F_{ext} and utilize the full formulation of eBTE to study the influence of this effect on the sign of magnetoresistance under a weak magnetic field.

With qualitative evaluations in the classical view, this nonlinear effect is originated from the multiplier of the angular derivative of velocity, which represents the influence of electric field on the velocity direction. This will reduce the frequency of the electrons scattering off the boundary, so the electric resistance and the negative magnetoresistance will be decreased as well. Figure 8 shows the phase diagram of the magnetoresistance curve for complete eBTE with a low electric field, which is quite similar to the linearized cases; however, when the electric field becomes larger whose dimensionless value is compared to the magnetic field ($E \sim v_{\mathrm{F}}B$), there will be no negative regimes from our numerical simulation results in this circumstance. Detailed examples are shown in Fig. 9.

Two points remain to be discussed here. First, the boundary condition is considered as an essential factor to account for the difference of the sign of magnetoresistance under different system setups [43]. Considering that the zero current condition requires that $j_y|_{y=0} = \int \chi(\boldsymbol{r}_0, \theta) \sin \theta \, d\theta = 0$ for any $\chi(\boldsymbol{r}_0, \theta)$, i.e., $\int_\pi^{-\pi} r(\theta, \theta') \sin \theta \, d\theta = 0$, the Fuchs

FIG. 7. Detailed magnetoresistance curves with different l_{MR} and l_{MC} values. (a) $l_{\mathrm{MR}} = 0.01$, i.e., the Ohmic regime. (b) $l_{\mathrm{MR}} = 1$. (c) $l_{\mathrm{MR}} = 100$, the hydrodynamic and/or ballistic regime. Dots are the DOM results, while the lines are guides for the eye.

enhances the bulk "nonlocal" scattering and reduces the effect of boundary scattering, which dramatically influences the sign of magnetoresistance as well and the occurrence of its maximum, which needs further detailed theoretical studies.
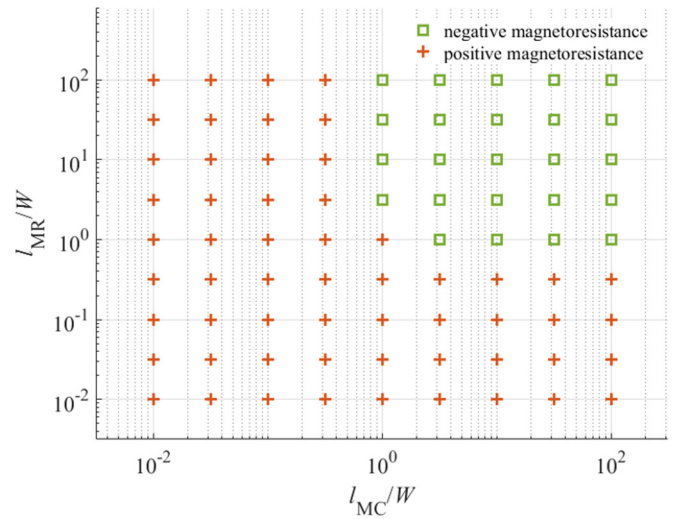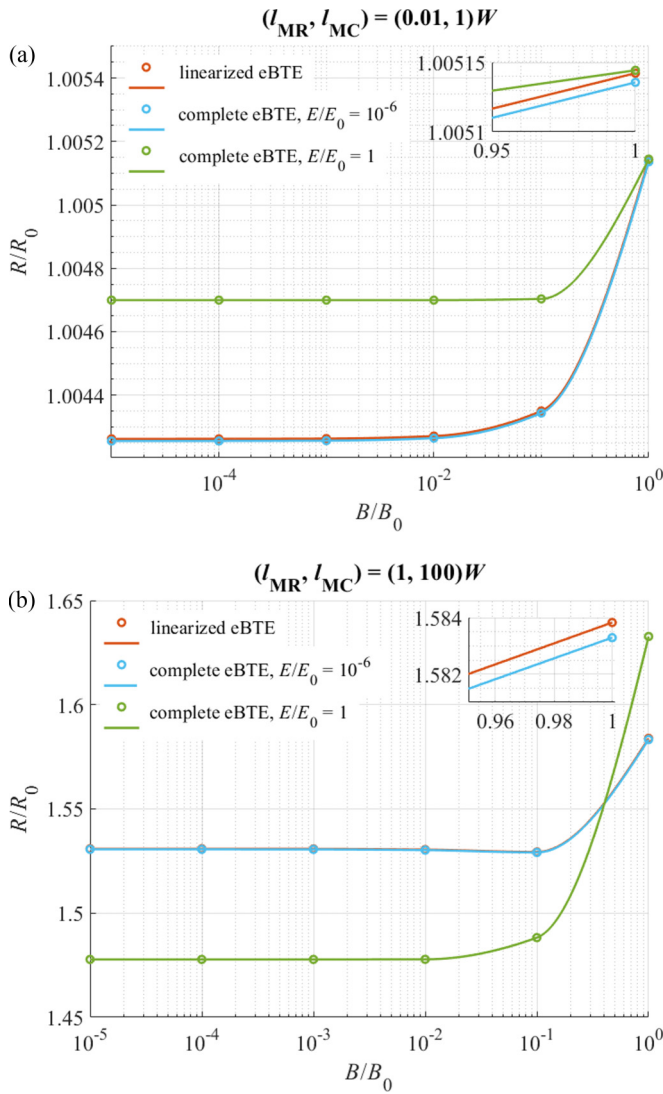
FIG. 9. Comparisons of the magnetoresistance curves between linearized eBTE and complete eBTE with different electric field strengths. Dots are the DOM results, while the lines are guides for the eye. It shows that the external electric field has a large impact on the monotonicity of the magnetoresistance curve.

boundary model utilized in this section satisfies this requirement. Through the analysis based on the macroscopic equations, it is believed that whether the electric current across the channel boundary is zero can dramatically impact the sign of magnetoresistance in the hydrodynamic regime, i.e., negative for zero current while positive for nonzero current [43]. However, our results show that even for the zero current cases, the magnetoresistance under weak magnetic fields is still positive. Thus it is indicated that the hydrodynamic description is not enough even for this simple case, with the ignorance of the contributions from the higher-order moments of the distribution function such as $M_3 = \int vvv(f - f^{eq})\frac{2}{(2\pi)^2}d^2k$ which has not been completely considered in the present macroscopic equations [12], and higher-order moment equations are required [71,91,92].

Second, there are various choices of models when dealing with the internal electric field. In our simulation, the

ordinary Poisson equation $\nabla \cdot E = (-e)n_\delta/\epsilon$ with uniform electrostatic potential in the out-of-plane direction is utilized, instead of the commonly used approximation called "local capacitance approximation" [19,93–98] $\phi \simeq (-e)n_\delta/\mathcal{C}$ due to the nonconvergence of the latter in some cases. Note that $\mathcal{C}$ is the local approximation of total capacitance including the geometrical capacitance of the device of interest $\mathcal{C}_g$ and the quantum capacitance from the pressure gradient $\mathcal{C}_Q$. For the limited cases that local capacitance approximation can work out, quite different results including the precise value of magnetoresistance and the convexity of the electron current profile are obtained. Considering that the electric current and internal electric field profile have been used to distinguish the flow regime of electron transport in the narrow channels [47–49], it is crucial to provide detailed explanations of the applicability of different internal electric models according to the experiment setup. In other words, the ballistic and/or hydrodynamic effect is not the only essential factor in the magnetoresistance effect, which also may be influenced by the internal electric field model chosen for compatibility with the experimental condition.

VI. CONCLUSIONS

In this paper, we have studied the magnetoresistance effect under a weak magnetic field and demonstrated that the negative magnetoresistance effect under a weak magnetic field occurs within the ballistic regime rather than the hydrodynamic regime, which also requires the external electric field to be low enough ($E \ll v_F B$). It is noteworthy that the existence of momentum-conserving scattering dramatically reverses the sign of magnetoresistance in the ballistic regime. When the external electric field becomes larger ($E \sim v_F B$), there will be only positive magnetoresistance for all l_{MR} and l_{MC}, which also addresses the necessity of incorporating the external electric field into the angular derivative term of electron Boltzmann transport equation. Our work sheds light on the influence of momentum-conserving scattering as well as the external electric field on the sign of magnetoresistance under a weak magnetic field.

APPENDIX A: DEDUCTION OF THE ITERATION SCHEME IN DOM ALGORITHM

As an integrodifferential equation with two derivative terms on the left and one integral term on the right, it is required to discretize both the two coordinates in the dimensionless displaced eBTE [Eq. (10)], i.e., the spatial coordinate in the real space (l.h.s.) and the angular coordinate for velocity (l.h.s. and r.h.s.). The spatial grid is uniform for the sake of simplicity, while the velocity angular grid is Gaussian to improve the accuracy and efficiency of the integration

procedure. The local real spatial and velocity angular grid size are denoted by dy and $\Delta_{\pm,j} = \pm(\varphi_{j\pm1} - \varphi_j)$, respectively.

In detail, the derivative terms are discretized using a first-order upwind scheme, a classical numerical scheme for the evolution equations in computational fluid dynamics. Taking the model equation $\partial u/\partial t = c\,\partial u/\partial x$ as an example, considering its discretization at the spatial-temporal grid point $(x_i, t^{(n)})$, the discrete formulation of the r.h.s. is written as follows:

$$\left(c\frac{\partial u}{\partial x}\right)_i = \begin{cases} c_i(u_{i+1}-u_i)/(x_{i+1}-x_i), & \text{if } c_i \leqslant 0 \\ c_i(u_i-u_{i-1})/(x_i-x_{i-1}), & \text{if } c_i > 0 \end{cases} \quad \text{(A1)}$$

which can be written into a more compact form:

$$\left(c\frac{\partial u}{\partial x}\right)_i = |c_i|\left(H(-c_i)\frac{u_i-u_{i+1}}{x_{i+1}-x_i} + H(c_i)\frac{u_i-u_{i-1}}{x_i-x_{i-1}}\right). \quad \text{(A2)}$$

Here $H(x)$ is the Heaviside function with the value 1 for $x > 0$ and 0 for $x \leqslant 0$. Then the complete formulation with uniform grid in space discretization and the first-order forward difference in time discretization is written as

$$u_i^{(n+1)} = u_i^{(n)} + \text{CFL}\big[H(-c_i)\big(u_i^{(n)} - u_{i+1}^{(n)}\big)$$
$$+ H(c_i)\big(u_i^{(n)} - u_{i-1}^{(n)}\big)\big], \quad \text{(A3)}$$

where $\text{CFL} := |c_i|(t^{(n+1)} - t^{(n)})/(x_{i+1} - x_i)$ is called the "Courant-Friedrichs-Lewy number", which determines the stability and convergence of the numerical scheme. Following the model formulation, $\sin\varphi$ (F_{ext}) and l_{eff} in Eq. (10) serve as c and t in the model equation, respectively, and the discrete form can be similarly obtained. The integration term in the scattering term [Eq. (6)] and the boundary condition [Eq. (8) with Eq. (9)] are calculated using Gaussian quadrature, which is a common technique in numerical analysis, and the discretized form of $P_i[\chi]$ ($i = 1, 2, 3$) is denoted by $\hat{P}_i[\chi]$ respectively.

As a result, the definition of numerical parameters in Eq. (11) is given by

$$\alpha = \frac{l_{\text{eff}}|\sin\varphi|}{dy},$$

$$\beta = l_{\text{eff}}|F_{\text{ext}}|\left(\frac{H(-F_{\text{ext}})}{\Delta_+} + \frac{H(F_{\text{ext}})}{\Delta_-}\right),$$

$$D_\alpha^{(n)} = \alpha\big(H(-\sin\varphi)\chi_{\text{up}}^{(n)} + H(\sin\varphi)\chi_{\text{down}}^{(n)}\big),$$

$$D_\beta^{(n)} = \beta\big(H(-F_{\text{ext}})\chi_{\text{a.w.}}^{(n)} + H(F_{\text{ext}})\chi_{\text{c.w.}}^{(n)}\big),$$

$$I_{\text{scat}}^{(n)} = \hat{P}_0\big[\chi_{\text{ctr}}^{(n)}\big] + \big(\hat{P}_1\big[\chi_{\text{ctr}}^{(n)}\big]\cos\varphi + \hat{P}_{-1}\big[\chi_{\text{ctr}}^{(n)}\big]\sin\varphi\big)\frac{l_{\text{eff}}}{l_{\text{MC}}}, \quad \text{(A4)}$$

where the subscripts "up/down" and "a.w./c.w." are the relative positions of the grids to the center point "ctr" in real space and velocity angular space, respectively.

In our numerical formulation, the dimensionless effective mean-free path l_{eff} plays a similar role to the time step, which indicates that the iteration is conducted with a time interval close to the minimum mean-free time of the system. The smaller l_{eff} is, the slower the convergence becomes, but with the enhanced numerical stability. The number of grid points

in the real space and angular space for velocity is chosen to be 2000 and 16, respectively, as a result of the grid size independence verification.

With regard to the comparison with other studies using discrete methods, one of the few papers we have found with algorithm details so far is de Jong and Molenkamp's [1]. They defined a local effective mean-free length which reduced the number of unknown variables and simplified the original displaced eBTE a great deal and then obtained the final solution through iteration. The number of grid points was at least 400 in their calculations for sufficient precision, and their results are used to verify our method. Note that the method of characteristics is utilized in the paper of Scaffidi et al. [81], but few details of the algorithm itself are given. The results are believed to be partly verified through the comparison with [1,88–90,99,100], which have been discussed in Sec. V A in detail.

APPENDIX B: DEDUCTION OF THE SOLUTION TO eNSE FOR TWO-DIMENSIONAL PARALLEL STEADY FLOW

Following the method in [12], the eNSE could be simplified to

$$\nu_{xx}\frac{d^2u}{dy} + \frac{(-e)}{m^*}E_x - \frac{u}{\tau_{\text{MR}}} = 0. \quad \text{(B1)}$$

The velocity slip condition derived from Fuchs boundary model is written as [63]

$$u|_{y=0} = l_b\frac{du}{dy}\bigg|_{y=0}, \qquad u|_{y=W} = -l_b\frac{du}{dy}\bigg|_{y=W} \quad \text{(B2)}$$

in which the kinematic viscosity coefficient and boundary slip length have the following form, and the coefficient error in the original literature has been corrected:

$$\nu_{xx} = \frac{1}{4}v_F l_{\text{eff}}, \qquad l_b = l_{\text{eff}}\frac{A}{3}\frac{1+p_s}{1-p_s}(A \doteq 0.995112). \quad \text{(B3)}$$

The solution is easy to find,

$$u = V_0 K\left[\lambda + \frac{(e^{\mu\tilde{y}}-1)(e^{\mu(1-\tilde{y})}-1)}{e^\mu-1}\right], \quad \text{(B4)}$$

where $\tilde{y} = y/W$, V_0 is the Drude velocity determined by the momentum-relaxing scattering rate τ_{MR} and K represents the synergistic effect of bulk and boundary scattering

$$V_0 = \frac{(-e)E_x\tau_{\text{MR}}}{m^*}, \qquad K = \frac{e^\mu(1+\lambda) + e^{-\mu}(1-\lambda) - 2}{e^\mu(1+\lambda)^2 - e^{-\mu}(1-\lambda)^2} \quad \text{(B5)}$$

in which the parameters λ, μ are defined by

$$\lambda = \frac{l_b}{\sqrt{\nu_{xx}\tau_{\text{MR}}}} = \frac{2A}{3}\frac{1+p_s}{1-p_s}\sqrt{\frac{\tilde{l}_{\text{eff}}}{\tilde{l}_{\text{MR}}}},$$

$$\mu = \frac{W}{\sqrt{\nu_{xx}\tau_{\text{MR}}}} = \frac{2}{\sqrt{\tilde{l}_{\text{eff}}\tilde{l}_{\text{MR}}}}. \quad \text{(B6)}$$

Notice that λ is proportional to the slip velocity and μ is the shape parameter, $\tilde{l}_{\text{eff (MR)}} = l_{\text{eff (MR)}}/W$. For example, while $\mu \ll 1$, i.e., $\tau_\nu \equiv W^2/\nu_{xx} \ll \tau_{\text{MR}}$, the velocity profile is almost parabolic, which is quite similar to the classical viscous fluid.

[1] M. J. de Jong and L. W. Molenkamp, Hydrodynamic electron flow in high-mobility wires, Phys. Rev. B **51**, 13389 (1995).

[2] R. Krishna Kumar, D. A. Bandurin, F. M. D. Pellegrino, Y. Cao, A. Principi, H. Guo, G. H. Auton, M. Ben Shalom, L. A. Ponomarenko, G. Falkovich, K. Watanabe, T. Taniguchi, I. V. Grigorieva, L. S. Levitov, M. Polini, and A. K. Geim, Superballistic flow of viscous electron fluid through graphene constrictions, Nat. Phys. **13**, 1182 (2017).

[3] D. A. Bandurin, A. V. Shytov, L. S. Levitov, R. K. Kumar, A. I. Berdyugin, M. Ben Shalom, I. V. Grigorieva, A. K. Geim, and G. Falkovich, Fluidity onset in graphene, Nat. Commun. **9**, 4533 (2018).

[4] R. N. Gurzhi, Minimum of resistance in impurity-free conductors, Sov. Phys. JETP **17**, 521 (1963).

[5] R. N. Gurzhi, Some features of the electrical conductivity of metals at low temperatures, Sov. Phys. JETP **20**, 953 (1965).

[6] R. N. Gurzhi, Hydrodynamic effects in solids at low temperature, Sov. Phys. Usp. **11**, 255 (1968).

[7] R. P. Gurzhi and S. I. Shevchenko, Hydrodynamic mechanism of electric conductivity of metals in a magnetic field, Sov. Phys. JETP **27**, 1019 (1968).

[8] R. N. Gurzhi, A. N. Kalinenko, A. I. Kopeliovich, and S. B. Rutkevich, Hydrodynamic effects in the electric conductivity of two-dimensional metals, Sov. Phys. JETP **17**, 521 (1986).

[9] R. N. Gurzhi, A. N. Kalinenko, and A. I. Kopeliovich, Hydrodynamic effects in the electrical conductivity of impure metals, Sov. Phys. JETP **69**, 863 (1989).

[10] I. Torre, A. Tomadin, A. K. Geim, and M. Polini, Nonlocal transport and the hydrodynamic shear viscosity in graphene, Phys. Rev. B **92**, 165433 (2015).

[11] L. Levitov and G. Falkovich, Electron viscosity, current vortices and negative nonlocal resistance in graphene, Nat. Phys. **12**, 672 (2016).

[12] F. M. D. Pellegrino, I. Torre, and M. Polini, Nonlocal transport and the Hall viscosity of two-dimensional hydrodynamic electron liquids, Phys. Rev. B **96**, 195401 (2017).

[13] A. D. Levin, G. M. Gusev, E. V. Levinson, Z. D. Kvon, and A. K. Bakarov, Vorticity-induced negative nonlocal resistance in a viscous two-dimensional electron system, Phys. Rev. B **97**, 245308 (2018).

[14] E. V. Gorbar, V. A. Miransky, I. A. Shovkovy, and P. O. Sukhachov, Nonlocal transport in Weyl semimetals in the hydrodynamic regime, Phys. Rev. B **98**, 035121 (2018).

[15] S. Danz and B. N. Narozhny, Vorticity of viscous electronic flow in graphene, 2D Materials **7**, 035001 (2020).

[16] H. Guo, E. Ilseven, G. Falkovich, and L. S. Levitov, Higher-than-ballistic conduction of viscous electron flows, Proc. Natl. Acad. Sci. USA **114**, 3068 (2017).

[17] H. Guo, E. Ilseven, G. Falkovich, and L. Levitov, Stokes paradox, back reflections and interaction-enhanced conduction, arXiv:1612.09239.

[18] M. Zarenia, I. Yudhistira, S. Adam, and G. Vignale, Enhanced hydrodynamic transport in near magic angle twisted bilayer graphene, Phys. Rev. B **101**, 045421 (2020).

[19] A. Gabbana, M. Polini, S. Succi, R. Tripiccione, and F. M. D. Pellegrino, Prospects for the Detection of Electronic Preturbulence in Graphene, Phys. Rev. Lett. **121**, 236602 (2018).

[20] D. Di Sante, J. Erdmenger, M. Greiter, I. Matthaiakakis, R. Meyer, D. R. Fernández, R. Thomale, E. van Loon, and T. Wehling, Turbulent hydrodynamics in strongly correlated Kagome metals, Nat. Commun. **11**, 3997 (2020).

[21] A. Dmitriev, M. Dyakonov, and R. Jullien, Classical mechanism for negative magnetoresistance in two dimensions, Phys. Rev. B **64**, 233321 (2001).

[22] A. T. Hatke, M. A. Zudov, J. L. Reno, L. N. Pfeiffer, and K. W. West, Giant negative magnetoresistance in high-mobility two-dimensional electron systems, Phys. Rev. B **85**, 081304(R) (2012).

[23] D. T. Son and B. Z. Spivak, Chiral anomaly and classical negative magnetoresistance of Weyl metals, Phys. Rev. B **88**, 104412 (2013).

[24] R. G. Mani, A. Kriisa, and W. Wegscheider, Size-dependent giant-magnetoresistance in millimeter scale GaAs/AlGaAs 2D electron devices, Sci. Rep. **3**, 2747 (2013).

[25] L. Bockhorn, A. Hodaei, D. Schuh, W. Wegscheider, and R. J. Haug, Magnetoresistance in a high mobility two-dimensional electron system as a function of sample geometry, J. Phys. Conf. Ser. **456**, 012003 (2013).

[26] Q. Shi, P. D. Martin, Q. A. Ebner, M. A. Zudov, L. N. Pfeiffer, and K. W. West, Colossal negative magnetoresistance in a two-dimensional electron gas, Phys. Rev. B **89**, 201301(R) (2014).

[27] J. Iñarrea, Theoretical model for negative giant magnetoresistance in ultrahigh-mobility 2D electron systems, EPL (Europhys. Lett.) **106**, 47005 (2014).

[28] P. S. Alekseev, Negative Magnetoresistance in Viscous Flow of Two-Dimensional Electrons, Phys. Rev. Lett. **117**, 166601 (2016).

[29] A. Lucas, R. A. Davison, and S. Sachdev, Hydrodynamic theory of thermoelectric transport and negative magnetoresistance in Weyl semimetals, Proc. Natl. Acad. Sci, USA **113**, 9463 (2016).

[30] R. L. Samaraweera, B. Gunawardana, T. R. Nanayakkara, R. C. Munasinghe, A. Kriisa, C. Reichl, W. Wegscheider, and R. G. Mani, Study of narrow negative magnetoresistance effect in ultra-high mobility GaAs/AlGaAs 2DES under microwave photo-excitation, Sci. Rep. **10**, 781 (2020).

[31] R. Menne and R. R. Gerhardts, Magnetoresistance of a two-dimensional electron gas with spatially periodic lateral modulations: Exact consequences of Boltzmann's equation, Phys. Rev. B **57**, 1707 (1998).

[32] A. D. Mirlin, D. G. Polyakov, F. Evers, and P. Wölfle, Quasi-classical Negative Magnetoresistance of a 2D Electron Gas: Interplay of Strong Scatterers and Smooth Disorder, Phys. Rev. Lett. **87**, 126805 (2001).

[33] A. Dmitriev, M. Dyakonov, and R. Jullien, Anomalous Low-Field Classical Magnetoresistance in Two Dimensions, Phys. Rev. Lett. **89**, 266804 (2002).

[34] L. Li, Y. Y. Proskuryakov, A. K. Savchenko, E. H. Linfield, and D. A. Ritchie, Magnetoresistance of a 2D Electron Gas Caused by Electron Interactions in the Transition from the Diffusive to the Ballistic Regime, Phys. Rev. Lett. **90**, 076802 (2003).

[35] I. V. Gornyi and A. D. Mirlin, Interaction-Induced Magnetoresistance: From the Diffusive to the Ballistic Regime, Phys. Rev. Lett. **90**, 076801 (2003).

[36] L. Bockhorn, P. Barthold, D. Schuh, W. Wegscheider, and R. J. Haug, Magnetoresistance in a high-mobility two-dimensional electron gas, Phys. Rev. B **83**, 113301 (2011).

[37] A. Levchenko, H.-Y. Xie, and A. V. Andreev, Viscous magnetoresistance of correlated electron liquids, Phys. Rev. B **95**, 121301(R) (2017).

[38] P. S. Alekseev, I. V. Gornyi, A. P. Dmitriev, V. Y. Kachorovskii, and M. A. Semina, Classical magnetoresistance of a two-component system induced by thermoelectric effects, Semiconductors **51**, 766 (2017).

[39] A. A. Patel, R. A. Davison, and A. Levchenko, Hydrodynamic flows of non-Fermi liquids: Magnetotransport and bilayer drag, Phys. Rev. B **96**, 205417 (2017).

[40] P. S. Alekseev, A. P. Dmitriev, I. V. Gornyi, V. Y. Kachorovskii, B. N. Narozhny, and M. Titov, Nonmonotonic magnetoresistance of a two-dimensional viscous electron-hole fluid in a confined geometry, Phys. Rev. B **97**, 085109 (2018).

[41] G. M. Gusev, A. D. Levin, E. V. Levinson, and A. K. Bakarov, Viscous electron flow in mesoscopic two-dimensional electron gas, AIP Adv. **8**, 025318 (2018).

[42] T. Holder, R. Queiroz, T. Scaffidi, N. Silberstein, A. Rozen, J. A. Sulpizio, L. Ella, S. Ilani, and A. Stern, Ballistic and hydrodynamic magnetotransport in narrow channels, Phys. Rev. B **100**, 245305 (2019).

[43] I. Mandal and A. Lucas, Sign of viscous magnetoresistance in electron fluids, Phys. Rev. B **101**, 045122 (2020).

[44] Z. Wang, M. Huang, J. Zhao, C. Chen, H. Huang, X. Wang, P. Liu, J. Wang, J. Xiang, C. Feng, Z. Zhang, X. Cui, Y. Lu, S. A. Yang, and B. Xiang, Fermi liquid behavior and colossal magnetoresistance in layered MoOCl$_2$, Phys. Rev. Materials **4**, 041001(R) (2020).

[45] G. M. Gusev, A. S. Jaroshevich, A. D. Levin, Z. D. Kvon, and A. K. Bakarov, Viscous magnetotransport and Gurzhi effect in bilayer electron system, Phys. Rev. B **103**, 075303 (2021).

[46] L. Ella, A. Rozen, J. Birkbeck, M. Ben-Shalom, D. Perello, J. Zultak, T. Taniguchi, K. Watanabe, A. K. Geim, S. Ilani, and J. A. Sulpizio, Simultaneous voltage and current density imaging of flowing electrons in two dimensions, Nat. Nanotechnol. **14**, 480 (2019).

[47] A. Jenkins, S. Baumann, H. Zhou, S. A. Meynell, D. Yang, K. Watanabe, T. Taniguchi, A. Lucas, A. F. Young, and A. C. Bleszynski Jayich, Imaging the breakdown of ohmic transport in graphene, arXiv:2002.05065.

[48] M. J. H. Ku, T. X. Zhou, Q. Li, Y. J. Shin, J. K. Shi, C. Burch, L. E. Anderson, A. T. Pierce, Y. Xie, A. Hamo, U. Vool, H. Zhang, F. Casola, T. Taniguchi, K. Watanabe, M. M. Fogler, P. Kim, A. Yacoby, and R. L. Walsworth, Imaging viscous flow of the Dirac fluid in graphene, Nature (London) **583**, 537 (2020).

[49] J. A. Sulpizio, L. Ella, A. Rozen, J. Birkbeck, D. J. Perello, D. Dutta, M. Ben-Shalom, T. Taniguchi, K. Watanabe, T. Holder, R. Queiroz, A. Principi, A. Stern, T. Scaffidi, A. K. Geim, and S. Ilani, Visualizing Poiseuille flow of hydrodynamic electrons, Nature (London) **576**, 75 (2019).

[50] K. E. Aidala, R. E. Parrott, T. Kramer, E. J. Heller, R. M. Westervelt, M. P. Hanson, and A. C. Gossard, Imaging magnetic focusing of coherent electron waves, Nat. Phys. **3**, 464 (2007).

[51] X. Liu, Y. X. Chong, R. Sharma, and J. C. Séamus Davis, Atomic-scale visualization of electronic fluid flow, Nat. Mater. (2021), doi: 10.1038/s41563-021-01077-1.

[52] S. Bhandari, G.-H. Lee, A. Klales, K. Watanabe, T. Taniguchi, E. Heller, P. Kim, and R. M. Westervelt, Imaging cyclotron orbits of electrons in graphene, Nano Lett. **16**, 1690 (2016).

[53] A. Hui, V. Oganesyan, and E.-A. Kim, Beyond Ohm's law: Bernoulli effect and streaming in electron hydrodynamics, Phys. Rev. B **103**, 235152 (2021).

[54] P. Cosme, J. S. Santos, and H. Terças, Hydrodynamic electrons in graphene: A viscous boundary-layer description, arXiv:2106.13783.

[55] P. Cosme, Nonlinear density waves in graphene electron fluid, arXiv:2106.14225 (2021).

[56] L. Bockhorn, I. V. Gornyi, D. Schuh, C. Reichl, W. Wegscheider, and R. J. Haug, Magnetoresistance induced by rare strong scatterers in a high-mobility two-dimensional electron gas, Phys. Rev. B **90**, 165434 (2014).

[57] P. S. Alekseev, A. P. Dmitriev, I. V. Gornyi, V. Y. Kachorovskii, B. N. Narozhny, and M. Titov, Counterflows in viscous electron-hole fluid, Phys. Rev. B **98**, 125111 (2018).

[58] B. N. Narozhny, I. V. Gornyi, M. Titov, M. Schütt, and A. D. Mirlin, Hydrodynamics in graphene: Linear-response transport, Phys. Rev. B **91**, 035414 (2015).

[59] F. M. D. Pellegrino, I. Torre, A. K. Geim, and M. Polini, Electron hydrodynamics dilemma: Whirlpools or no whirlpools, Phys. Rev. B **94**, 155414 (2016).

[60] G. Falkovich and L. Levitov, Linking Spatial Distributions of Potential and Current in Viscous Electronics, Phys. Rev. Lett. **119**, 066601 (2017).

[61] R. Moessner, P. Surówka, and P. Witkowski, Pulsating flow and boundary layers in viscous electronic hydrodynamics, Phys. Rev. B **97**, 161112 (2018).

[62] G. Wagner, Boundary conditions for electron flow in graphene in the hydrodynamic regime, arXiv:1509.07113.

[63] P. S. Alekseev and M. A. Semina, Ballistic flow of two-dimensional interacting electrons, Phys. Rev. B **98**, 165412 (2018).

[64] P. S. Alekseev and A. P. Dmitriev, Viscosity of two-dimensional electrons, Phys. Rev. B **102**, 241409(R) (2020).

[65] R. Q. Hood and L. M. Falicov, Boltzmann-equation approach to the negative magnetoresistance of ferromagnetic–normal-metal multilayers, Phys. Rev. B **46**, 8287 (1992).

[66] A. Lucas, Kinetic theory of Electronic Transport in Random Magnetic Fields, Phys. Rev. Lett. **120**, 116603 (2018).

[67] M. S. Steinberg, Viscosity of the electron gas in metals, Phys. Rev. **109**, 1486 (1958).

[68] P. L. Bhatnagar, E. P. Gross, and M. Krook, A model for collision processes in gases. I. Small amplitude processes in charged and neutral one-component systems, Phys. Rev. **94**, 511 (1954).

[69] J. Callaway, Model for lattice thermal conductivity at low temperatures, Phys. Rev. **113**, 1046 (1959).

[70] Y. Guo and M. Wang, Phonon hydrodynamics for nanoscale heat transport at ordinary temperatures, Phys. Rev. B **97**, 035421 (2018).

[71] Y. Guo and M. Wang, Phonon hydrodynamics and its applications in nanoscale heat transport, Phys. Rep. **595**, 1 (2015).

[72] K. Fuchs, The conductivity of thin metallic films according to the electron theory of metals, Mathematical Proceedings of the Cambridge Philosophical Society **34**, 100 (1938).

[73] S. B. Soffer, Statistical model for the size effect in electrical conduction, J. Appl. Phys. **38**, 1710 (1967).

[74] F. Toschi, P. Vignolo, S. Succi, and M. P. Tosi, Dynamics of trapped two-component Fermi gas: Temperature dependence of the transition from collisionless to collisional regime, Phys. Rev. A **67**, 041605 (2003).

[75] A. O. Govorov and J. J. Heremans, Hydrodynamic Effects in Interacting Fermi Electron Jets, Phys. Rev. Lett. **92**, 026803 (2004).

[76] S. Riedl, E. R. Sánchez Guajardo, C. Kohstall, A. Altmeyer, M. J. Wright, J. H. Denschlag, R. Grimm, G. M. Bruun, and H. Smith, Collective oscillations of a Fermi gas in the unitarity limit: Temperature effects and the role of pair correlations, Phys. Rev. A **78**, 053609 (2008).

[77] T. Lepers, D. Davesne, S. Chiacchiera, and M. Urban, Numerical solution of the Boltzmann equation for the collective modes of trapped Fermi gases, Phys. Rev. A **82**, 023609 (2010).

[78] O. Goulko, F. Chevy, and C. Lobo, Collision of two spin-polarized fermionic clouds, Phys. Rev. A **84**, 051605(R) (2011).

[79] O. Goulko, F. Chevy, and C. Lobo, Boltzmann equation simulation for a trapped Fermi gas of atoms, New J. Phys. **14**, 073036 (2012).

[80] P.-A. Pantel, D. Davesne, and M. Urban, Numerical solution of the Boltzmann equation for trapped Fermi gases with in-medium effects, Phys. Rev. A **91**, 013627 (2015).

[81] T. Scaffidi, N. Nandi, B. Schmidt, A. P. Mackenzie, and J. E. Moore, Hydrodynamic Electron Flow and Hall Viscosity, Phys. Rev. Lett. **118**, 226601 (2017).

[82] S. Chiacchiera, D. Davesne, and M. Urban, Shock waves in colliding Fermi gases at finite temperature, Phys. Rev. A **98**, 053622 (2018).

[83] R. C. V. Coelho and M. M. Doria, Lattice Boltzmann method for semiclassical fluids, Comput. Fluids **165**, 144 (2018).

[84] M. Chandra, G. Kataria, D. Sahdev, and R. Sundararaman, Hydrodynamic and ballistic AC transport in two-dimensional Fermi liquids, Phys. Rev. B **99**, 165409 (2019).

[85] M. Chandra, G. Kataria, and D. Sahdev, Quantum critical ballistic transport in two-dimensional Fermi liquids, arXiv:1910.13737.

[86] Y. Guo and M. Wang, Heat transport in two-dimensional materials by directly solving the phonon Boltzmann equation under Callaway's dual relaxation model, Phys. Rev. B **96**, 134312 (2017).

[87] X. Ran and M. Wang, Efficiency improvement of discrete-ordinates method for interfacial phonon transport by Gauss-Legendre integral for frequency domain, J. Comput. Phys. **399**, 108920 (2019).

[88] E. Ditlefsen and J. Lothe, Theory of size effects in electrical conductivity, Philos. Mag. **14**, 759 (1966).

[89] E. H. Sondheimer, The influence of a transverse magnetic field on the conductivity of thin metallic films, Phys. Rev. **80**, 401 (1950).

[90] E. H. Sondheimer, Influence of a magnetic field on the conductivity of thin metallic films, Nature (London) **164**, 920 (1949).

[91] J. Dufty, K. Luo, and J. Wrighton, Generalized hydrodynamics revisited, Phys. Rev. Res. **2**, 023036 (2020).

[92] B. N. Narozhny, Electronic hydrodynamics in graphene, Ann. Phys. **411**, 167979 (2019).

[93] D. A. Bandurin, I. Torre, R. K. Kumar, M. Ben Shalom, A. Tomadin, A. Principi, G. H. Auton, E. Khestanova, K. S. Novoselov, I. V. Grigorieva, L. A. Ponomarenko, A. K. Geim, and M. Polini, Negative local resistance caused by viscous electron backflow in graphene, Science **351**, 1055 (2016).

[94] M. Dyakonov and M. Shur, Shallow Water Analogy for a Ballistic Field Effect Transistor: New Mechanism of Plasma Wave Generation by Dc Current, Phys. Rev. Lett. **71**, 2465 (1993).

[95] M. I. Dyakonov and M. S. Shur, Choking of electron flow: A mechanism of current saturation in field-effect transistors, Phys. Rev. B **51**, 14341 (1995).

[96] A. Tomadin and M. Polini, Theory of the plasma-wave photoresponse of a gated graphene sheet, Phys. Rev. B **88**, 205426 (2013).

[97] A. Tomadin, G. Vignale, and M. Polini, Corbino Disk Viscometer for 2D Quantum Electron Liquids, Phys. Rev. Lett. **113**, 235901 (2014).

[98] M. Dyakonov and M. Shur, Detection, mixing, and frequency multiplication of terahertz radiation by two-dimensional electronic fluid, IEEE Trans. Electron Devices **43**, 380 (1996).

[99] D. K. C. Macdonald, K. Sarginson, and F. E. Simon, Size effect variation of the electrical conductivity of metals, Proc. R. Soc. Lond. A **203**, 223 (1950).

[100] E. H. Sondheimer, The mean free path of electrons in metals, Adv. Phys. **1**, 1 (1952).